

---

# Learning Action-Conditional and Object-Centric Gaussian Splatting World Models for Rigid Objects

---

Jens U. Kreber   Lukas Mack   Joerg Stueckler

Intelligent Perception in Technical Systems Group

University of Augsburg

Augsburg, Germany

{jens.kreber, lukas.mack, joerg.stueckler}@uni-a.de

## Abstract

World models enable intelligent agents to predict the consequences of their actions on the environment. In this paper, we propose Multi Rigid Object Gaussian World Model (MRO-GWM), a novel model that learns action-conditional dynamics of rigid objects in 3D. By representing the scene by object-centric Gaussians, we can represent arbitrary object shapes and multi-object scenes. We develop a novel spatio-temporal transformer architecture that predicts future rigid body motion from a history of object Gaussians and future actions. Objects are represented by their Gaussians in a canonical frame, which allows for describing object motion as rigid body transformation. Our model is trained on reconstructions from multiple viewpoints, which requires the model to handle partial observations of objects due to occlusions. We analyze prediction performance of our approach on synthetic datasets composed of typical household objects with multi-object dynamics and interactions by a robot end effector. We also evaluate our model in model-predictive control for non-prehensile manipulation in simulation.

## 1 Introduction

World models allow intelligent agents to predict the consequences of potential actions in perceived scenes and thereby enable them to plan ahead. They capture task-agnostic properties of the world and therefore form a keystone of their generalization abilities. A challenging domain are the rigid-body dynamics in everyday household scenes where many objects of highly varying shapes are closely placed next to each other. An interaction with one object might have effect on surrounding ones and the objects might not be fully observable due to occlusions. Our novel Multi Rigid Object Gaussian World Model (MRO-GWM) learns the dynamics in this setting end-to-end, operating on an object-centric 2D Gaussian splatting representation of the scene. To this end, we propose a novel spatio-temporal transformer architecture which predicts future object poses and is conditioned on a history of object and end-effector Gaussians. The history of Gaussians are obtained by transforming per-object representations by rigid object and end-effector poses. We evaluate our method on simulated tabletop scenes containing closely placed household objects of varying shapes. We compare model variants and ablations regarding prediction performance on unseen objects. Finally, we evaluate model-predictive control with our model in simulation for two non-prehensile manipulation tasks and demonstrate that it can successfully solve the tasks in several multi-object scenes<sup>1</sup>. Our contributions are as follows: (1) We propose to use object-centric Gaussian splatting [38] as scene representation and per-object rigid transforms to encode a history of pose observations. (2) We introduce a novel transformer architecture that operates on this representation using temporal and spatial blocks as well as a new spatio-temporal attention layer. (3) We integrate and demonstrate our world model for model-predictive control in non-prehensile manipulation.

<sup>1</sup>Videos are available at the project website <https://embodiedvision.github.io/mro-gwm/>

## 2 Related Work

Several approaches for learning world models have been proposed in recent years in the machine learning, robot learning, and computer vision communities. One approach is to learn action-conditional video prediction models [10, 4]. The approach in [8] learns a 3D world model for multi-object interactions, but uses implicit NeRF representations of object shape. Gaussian representations provide an alternative explicit 3D representation which has recently attracted attention.

**Integrating physics models with Gaussians.** PIN-WM [17] use differentiable rendering of Gaussians and differentiable physics to infer physical parameters from visual observations. Dynamics simulation is achieved using a differentiable LCP formulation [7]. The model is used to train policies, but differently to our approach only single-object scenes are considered. ContactGaussian-WM [29] uses a complementary-free differentiable physics engine to propagate objects represented by 3D Gaussians. Rigid objects and deformables are simulated in a differentiable particle physics simulation by Embodied Gaussians [1]. In this approach, Gaussians for visual scene representation are coupled with particles of a point-based dynamics simulation. Visual reconstruction errors are mapped to physical forces on the particles for object tracking. Related approaches, such as [35, 32, 36], integrate physics simulation using the material point method [12] for deformables into a 3D Gaussian reconstruction of a scene. Physics-based simulation is, however, restricted to the model class of the simulator and cannot cope with strong violations of the physical model. Also, differently to our learning-based dynamics model, these approaches require that the scene and object shapes are fully known or observed so that physical simulation becomes feasible.

**Predicting neural physical dynamics for Gaussians.** 3DGSim [37] trains transformers for simulating the dynamics of single objects represented as 3D Gaussians but is not action-conditional like our approach. The transformer aggregates unstructured pointclouds from multiple timesteps into a single-step per-point prediction. Our approach uses a spatial aggregation whose structure is shared over time and predicts multi-step per-object pose changes. Zhang et al. [34] use graph neural networks to learn a single-step, action-conditional dynamics model for Gaussian representations of single objects such as deformables and use the model for planning non-prehensile manipulation. Our world model predicts the motion of multiple objects which are represented as Gaussians. ManiGaussian [19, 33] also learn a single-step prediction model for Gaussians which are estimated from image observations using multi-head neural networks. The prediction model is implemented by a fully connected neural network and predicts translation and rotation for each Gaussian. The model is demonstrated as visual 3D representation for imitation learning. The approach in [22] predicts the motion of Gaussians in a single step and uses the predictions for failure detection during the execution of motion plans. Latent diffusion transformers are applied in [20] for predicting the motion of Gaussians in a single step, which is used for model-based reinforcement learning. Tseng et al. [27] use GNNs to learn an action-conditional dynamics model for granular media represented as Gaussians. Gradient-based model-predictive control is used to align the current Gaussians with a target configuration. GAF [6] predict Gaussian representations for the current image, a future state, and also the scene flow between the current and future Gaussians. The robot action between the Gaussian representations is estimated from the end-effector Gaussians. The learned representation is used for imitation learning. Differently to the above approaches, our approach estimates an object-centric Gaussian scene representation and predicts rigid body motion of the objects in single steps using a transformer architecture. Our transformer includes a novel spatio-temporal attention for taking the shape and contacts between objects into account. We demonstrate our approach for several non-prehensile manipulation tasks. Neural Gaussian Force Fields [16] learn an object-centric dynamics model for multi-object scenes. They predict forces acting on objects with a neural interaction network architecture and use ODE solvers to determine the motion of objects and also individual Gaussians to predict object deformations. Contrary to our approach, they do not model robot actions as end-effector motions, but can model external forces. Additionally, the approach uses a shape completion method to fill in occlusions in a feed-forward multi-view Gaussian reconstruction. We use a transformer model with spatial aggregation, spatial and temporal attention layers which implicitly models unobserved parts.

## 3 Method

To represent the scene, we follow ObjectGS [38] and use object-aware Gaussian splatting [14], where each Gaussian is associated with an object. This representation allows for applying rigid-body

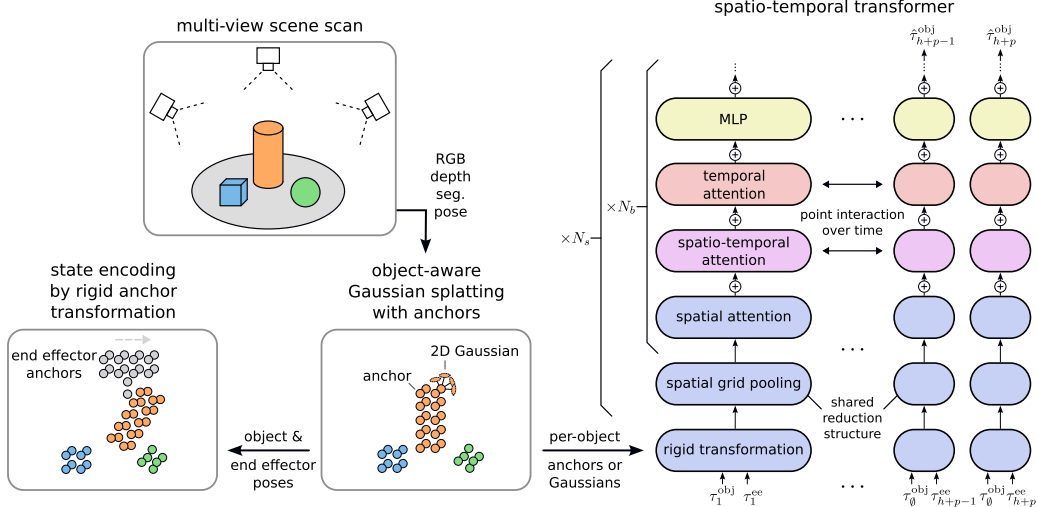


Figure 1: Method overview. Left: Proposed scene representation: Per-object anchors or Gaussians are obtained by object-centric Gaussian splatting. They are rigidly transformed to encode the history of scene states given object and end-effector poses. Right: Proposed spatio-temporal transformer: Spatial grid pooling and spatial attention blocks are combined with temporal attention between points and a newly proposed spatio-temporal attention layer. Given a history and future end-effector poses, future object poses are predicted.  $\hat{\tau}_i^{\text{obj}}$  indicates predicted object poses and  $\tau_0^{\text{obj}}$  a fixed dummy pose.

transformations to each group of Gaussians and model the scene in varying object poses. We use these transformed scene representations (observed history of object movement and future end-effector poses) to condition our model and predict the resulting future object pose trajectories given the end-effector actions. Concretely, we assume access to multiple posed RGB-D images of the scene  $I \subset \mathbb{R}^{n_{\text{img}} \times w_{\text{img}} \times h_{\text{img}} \times 4}$  with corresponding camera poses in the world frame  $\xi_i^{\text{cam}} \in \text{SE}(3)$ . We assume corresponding object segmentation masks  $O \subset \mathbb{N}^{n_{\text{img}} \times w_{\text{img}} \times h_{\text{img}} \times N_{\text{obj}}}$  to be known and use ground-truth masks in our experiments. During interaction of the robot with the scene, at each timestep, we assume that the poses of the objects  $\xi_i^{\text{obj}} \in \text{SE}(3)$  and the end-effector pose  $\xi^{\text{robot}}$  are also known. For both, we use ground-truth poses provided by the simulator in our experiments. We leave integrating object segmentation and pose estimation with our dynamics modeling approach to future work. Given a history of SE(3) poses of the objects  $\tau_{1:h}^{\text{obj}} := \tau_1^{\text{obj}}, \dots, \tau_h^{\text{obj}}$  and the end-effector in world coordinates and a trajectory of future end-effector poses  $\tau_{h+1:h+p}^{\text{ee}}$ , our model predicts future SE(3) poses  $\tau_{h+1:h+p}^{\text{obj}}$  of the objects.

### 3.1 Scene Representation With Object-Aware Gaussian Splatting

ObjectGS is an extension of ScaffoldGS [21], which does not optimize 3D Gaussians directly, but represents the scene by a grid of voxels (called "anchors") with latent features. From each anchor, a fixed number of Gaussians is decoded with an MLP and optimized with a splatting rendering loss. ScaffoldGS demonstrates that this provides a compressed representation, while maintaining similar reconstruction quality than direct Gaussian splatting. ObjectGS itself introduces object awareness into the process, using an object segmentation mask for each image. Each anchor has a unique object id shared by the decoded Gaussians. These object ids are also rendered and included in the optimization process so that a loss against the actual segmentation mask is minimized. As a result, anchors (and thereby decoded Gaussians) can be uniquely assigned to an object, which we use for rigid-body scene transformations. To initialize the anchors, ObjectGS first performs a voting on an initial point cloud of the scene to uniquely determine the object id per point. Each point is projected into each camera view and, if contained in the image, given a vote for the object id at the corresponding pixel in the object segmentation mask. We extend this voting scheme by additionally comparing the projected depth with the actual depth observation and require the mismatch to be smaller than 1 cm for the vote to count. Since we consider scenes with closely populated objects which leads to occlusions, this ensures that each camera view votes only for an object it actually sees. We then proceed similarly to

ObjectGS in the 2D Gaussian splatting variant [13], which we observed to represent surfaces better than 3D Gaussians [38] in our setting.

Our model supports two input options, firstly the properties of 2D Gaussians directly (position, rotation, scale, opacity). Alternatively, it can operate on the anchors, which store similar information, but in a neurally compressed way. To enable the model to work on a consistent latent space, we extend [38] to the multi-scene setting: We share the MLPs for scale, rotation, and opacity over training scenes, but use a distinct MLP for color encoding per scene. We split the anchor features (32 originally) into 16 for spatial information (scale, rotation, opacity) and 16 for color. Our model then only operates on the former 16 features, ignoring the color features. For validation and testing scenes, we re-use the previously trained shared MLPs to splat the scenes. Additionally, we render multiple views of a robot end effector and splat it in a similar way. This allows us to place the end effector spatially into the scene and vary its pose. Note that we use distinct MLPs to splat the end effector, as the specialized MLP reconstructs the end effector with higher quality. We did not observe a significant loss in prediction performance compared to using the shared MLP from the training scenes. For the variant operating on explicit 2D Gaussians, the approach is analogously, but without any shared MLPs. ScaffoldGS allows for view-dependent Gaussian decoding, which is not suitable in our setting, since the scene representation should be view-independent for dynamics modeling. Thus, we use the view-independent parts of the decoding process only.

### 3.2 Spatio-Temporal Transformer

**Input** To encode the observed history of object trajectories and end-effector actions, for each timestep we transform all anchors or Gaussians corresponding to the respective object or end effector by its respective pose. For each timestep in the prediction horizon, we also transform the end-effector representation according to the input actions, while leaving the object representations at a fixed position. Denoting the history length by  $h$  and the prediction horizon by  $p$ , this results in  $h + p$  spatially differently transformed scene representations. Our model operates on these along a temporal and a spatial axis. Anchors are transformed by transforming their spatial location. Apart from their location, they contain spatial offsets to the corresponding Gaussians, scaling parameters and latent features. We rotate the offsets according to the transformation and concatenate them to the scaling and latent features. Since anchors by themselves do not have a notion of orientation, we encode their rotation by a quaternion and use it as additional feature. For the 2D Gaussians, we apply the spatial transformations. We use their rotation, opacity and scaling as feature. For both anchors and Gaussians, we embed the corresponding object index and a Boolean representing if it is part of a history or future timestep and concatenate these as features. The scene representation can have a large spatial extent due to the background being included. However, we know that interactions can only occur around objects. We therefore filter out background anchor that are further than some threshold (10 cm in our experiments) away from object or end-effector anchors. This filtering also applies when operating on explicit Gaussians and they are decoded from remaining anchors.

**Architecture** To process the spatial representation, we treat the transformed anchors or Gaussians as points with features and build on components of PTv2 [30] to operate on them. Most importantly, PTv2 uses a spatial attention mechanism, where neighboring points exchange information. For each point, an attention is computed over its  $k$ -nearest neighbors, which includes their spatial relation. Features from all neighbors are scaled by the attention and summed up to update the point feature. Additionally, points are pooled based on spatial grids with increasing grid cell size. Our model consists of multiple stages, where each stage  $s_i$  processes the transformed representations for all timesteps simultaneously. Each stage has the form  $s_i = b_{i, N_{\text{blocks}}} \circ \dots \circ b_{i, 1} \circ \text{pe} \circ \text{pool}_i$ . The pooling  $\text{pool}_i$  is similar to the one described in PTv2, where features from points in the same grid cell are combined and the respective coordinates are averaged. Importantly, we perform the pooling per object independently including the background. Since the spatial structure between time steps differs only by rigid transformations of per-object points, we calculate which points are pooled together once for all grid cell sizes and objects at the first timestep only. Then we apply identical per-object pooling operations for all time steps. This has two benefits: it saves computational effort and also, each point has correspondences even at higher stages with fewer pooled points between all timesteps. We exploit this to have points also exchange information over time with their counterparts at other time steps, as we will detail below. After the pooling, a standard sinusoidal positional embedding  $\text{pe}$  [28] encoding the time index is added to all features. Following the architecture of DiT [23], subsequently multiple

residual blocks  $b_{i,j}$  with several residual layers are applied before proceeding to the next stage. Each block contains the following four layer types: As in DiT, we use standard attention [28] over time, meaning that each point exchanges information with their counterparts at different time steps, i.e., no information flows over the spatial axis, and a pointwise MLP layer. We also use the spatial vector attention layer from PTv2, where information is exchanged between neighboring points. During this operation, no information flows over the temporal axis. Lastly, we use a new temporal-spatial attention layer that uses the same mechanism as the PTv2 spatial attention, only that the neighbors are now the point counterparts at different time steps. This directly provides information about the relative motion of each point for the attention calculation. We stack the layers in the following order: spatial attn.  $\rightarrow$  temporal-spatial attn.  $\rightarrow$  temporal attn.  $\rightarrow$  MLP. For the last stage, we choose a grid cell size that spans the whole scene. Since aggregation is done per object, this means that only one point per object remains. After the stage, the points for background and end-effector are discarded and a final linear layer maps the features of all points corresponding to an object to the prediction. For more details and used hyperparameters, refer to appendix section C.

**Prediction representation and losses** We train our model to predict the relative motion in position and orientation in world coordinates between two timesteps across the prediction horizon for each object. Integration from the last history timestep yields predicted pose trajectories. Following [9], we represent rotations as 9D rotation matrices and apply orthogonalization on the predictions to achieve valid 3D rotations. Since we predict relative rotation, which is often small, we apply the following normalization scheme: From a ground-truth relative rotation matrix  $\mathbf{R} \in SO(3)$ , we subtract the identity matrix and divide each component by its standard deviation over the training set, i.e.  $\tilde{\mathbf{R}} = (\mathbf{R} - \mathbf{I}) \div \Sigma_{\text{rot}}$  where  $\div$  represents element-wise division and  $\Sigma_{\text{rot}}$  contains the element-wise standard deviations of  $\mathbf{R} - \mathbf{I}$  over the training set. We aim at predicting  $\tilde{\mathbf{R}}$  by the network and compute the loss with an l2 norm between the matrices. To obtain a valid rotation from a network prediction, the normalization process is reversed and the resulting matrix orthogonalized. For the relative position, we divide the ground truth motion by its mean norm over the training set and compute the squared l2 norm against the prediction.

## 4 Experiments

### 4.1 Experiment Setup

**Scene generation and datasets** We train and evaluate our model on datasets obtained using the Maniskill simulator [26]. We consider a tabletop scene populated with varying counts of 1 to 5 of objects from the YCB model dataset [5] which are provided as Maniskill assets. We generate scenes where objects are closely positioned next to each other and likely interacting during manipulation by the robot. To this end, we develop a sampling procedure that is detailed in appendix section A. As we want to evaluate how well our model generalizes to unseen objects, we use disjoint object pools for training, validation, and testing datasets. For each generated scene, objects are randomly sampled from the respective pool. To assess how important variation in objects seen during training is for model performance, we create one training set that exclusively contains 16 objects from the 21 objects used in [31] called YCB-V, which are a subset of the whole YCB set. The remaining 5 YCB-V objects are used as pool for our validation dataset. For the testing pool, we randomly select one object from each of the five categories proposed by YCB [5] excluding YCB-V. Our remaining training datasets termed YCB use the remaining pool (whole YCB set excluding test and validation set) of 65 YCB objects.

For our training and validation sets, we generate additional augmented scenes to the initially sampled scenes. We generate multiple object pose layouts that use the exact same objects, but otherwise undergo the same pose sampling procedure and interaction data collection. For these layouts, we use the same splatting representation obtained from the initial scene, since only object poses are changed. Thereby we obtain more interaction data with the same number of splatted scenes. Our main training set, termed YCB-100-100, contains 100 original scenes and 100 augmented layouts per original scene. To study the effect of the number of original scenes and number of augmented layouts, we create two different variants, YCB-50-200 and YCB-200-50 that contain different ratios of original scenes and augmentations (second number). As a training dataset with a smaller object pool, we construct YCBV-100-100 drawing from the aforementioned YCB-V training pool of 16 objects. As validation set, we use a YCBV-20-20 set. For prediction evaluation we systematically

create a test set with 20 scenes for each object count from 1 to 5, resulting in 100 scenes total. We do not use layout augmentations, but sample 3 different interaction trajectories. For planning evaluation, we create 8 scenes per object count, resulting in 40 in total. To capture the scene, we obtain 32 images viewing the scene center from elevation angles  $30^\circ$  and  $60^\circ$ , constant radius 0.4 m and equally spaced azimuth angles in the full  $360^\circ$  range. For one ablation, we consider data obtained with azimuth angles ranging only to  $180^\circ$ . We use the rendered object masks and depths from the images for splatting. To obtain an initial point cloud to initialize the anchors, we project the camera pixels into 3D using this depth information. We perform object-aware Gaussian splatting as described above with an anchor resolution of 1 cm for 5,000 steps. We model a Franka panda robot with a stick-like end-effector in the scene, similarly to the tasks already shipped with Maniskill and use an end-effector position controller in 3D for inverse kinematics. To generate interaction data, we use a heuristic to target interesting points around objects. See appendix section A for more details. We generate linearly interpolated trajectories towards target points. The interpolated points are sent as actions to the low-level position controller and are also recorded as input for the model during training. We interact with the simulator at 20 Hz, while the simulation runs at 100 Hz (Maniskill defaults). After executing an action, we record the resulting object poses.

**Model training** We implement our model in PyTorch [3] and train it with the AdamW [18] optimizer with default parameters for 60,000 steps. We use a half-period cosine learning rate schedule with 3,000 warmup steps and a base learning rate of  $4.4 \cdot 10^{-4}$ . As training examples, we split the recorded interaction trajectories into small chunks according to the model’s prediction horizon (default  $p = 4$ ) and step resolution (default 5 Hz). We use a fixed history size of  $h = 3$ . For each randomly sampled chunk, we load the corresponding scene representation it was recorded in. We conduct training with a batch size of 30. Our default model ( $p = 4$ , 5 Hz, trained on YCB-100-100) takes approximately 22 h on a cluster node with one Nvidia A40 GPU to train. For inference, one batch of 30 items takes 0.65 s on average to compute on the validation set.

**Prediction performance evaluation** To assess the prediction performance of a model, we evaluate it on the test set described above. We sample trajectory chunks from the dataset of varying sizes that require different counts of recurrent model calls (predicted object poses are used as history for subsequent invocations). We compare the predicted poses at certain prediction horizons with the ground truth ones. To this end, we report the Euclidean distance between positions and the geodesic angle between the rotations. We provide a study on variants and ablations of our model to assess design choices. Since there is no other work available that allows for direct comparison in our setting of multi-object dynamics with partial observations. For [8], which is closest in setting, there is no code available. The multi-object dynamics learning approach in [16] does not directly support conditioning on end-effector position actions.

**Planning performance evaluation** To evaluate if the learned world model can be used for planning robot actions, we embed it into model-predictive control (MPC) for non-prehensile manipulation. We implement a variant of iCEM [25] for sampling-based optimization of keypoint-parametrized end-effector trajectories that minimizes a set of task-specific costs over a planning horizon. The end-effector keypoints are linearly interpolated at a constant velocity before being passed to the model for predicting the resulting object-pose trajectories. Planning is repeated at 2 Hz where each planning iteration performs a single optimization iteration that updates the mean but not the covariance of the sample distribution to ensure constant exploration. The sampling-based MPC framework containing the model is evaluated on two different tasks, i.e., pushing objects to goal positions and clearing an area in the middle of the table. For each task, the planner is initialized with the identical parameter configuration but with a varying set of task-specific cost functions. The performance in each task is evaluated over the 40 scenes in the planning test dataset and with 5 episodes per scene. For tasks with varying goals, a goal is sampled per episode. Further details can be found in the appendix section B.

## 4.2 Prediction Results

In Figure 2, we analyze the prediction performance in position and rotation error and of model variants with different time resolution and prediction horizons. We distinguish results considering all errors at the prediction horizon and those where a ground truth movement (pos. change  $> 1 \cdot 10^{-4}$  m, rot. change  $> 1 \cdot 10^{-2}$  rad for single step) happens during the horizon for the considered object. The large differences between these plots and the large spread between 25% and 75% quantiles illustrates

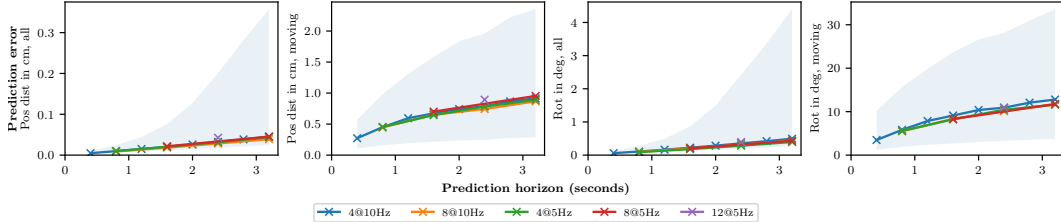


Figure 2: Prediction errors over horizon for different model variants, considering either all poses at the prediction horizon or only those where a ground truth movement for the respective object occurs during the horizon. Indicated are median prediction errors of model variants and the area between the 25% and 75% quantile of the 4@10Hz variant. Predictions of 5 model training seeds were used. We observe that model variants with different prediction horizons and step granularity perform similarly for the same time horizon.

Variant	Median pos err in cm	Mean pos err in cm	Median rot err in deg	Mean rot err in deg
Train set YCB-100-100 (main)	<b>0.45</b> (0.01)	<b>0.73</b> (0.01)	<b>5.54</b> (0.27)	<b>7.08</b> (0.05)
Train set YCB-50-200	0.46 (0.01)	0.75 (0.01)	6.25 (0.30)	7.14 (0.09)
Train set YCB-200-50	0.47 (0.01)	0.75 (0.02)	5.86 (0.36)	7.14 (0.09)
Train set YCBV-100-100	0.52 (0.04)	0.83 (0.06)	5.75 (0.35)	7.84 (0.13)
Anchor size 0.005	0.47 (0.02)	0.75 (0.02)	5.56 (0.09)	7.15 (0.07)
Anchor size 0.02	0.48 (0.02)	0.76 (0.01)	5.87 (0.44)	7.20 (0.10)
Explicit Gaussians	0.48 (0.02)	0.76 (0.02)	5.80 (0.22)	7.11 (0.08)
Limited view	0.47 (0.01)	0.75 (0.02)	5.98 (0.22)	7.27 (0.05)
No spatio-temporal attn.	0.49 (0.01)	0.77 (0.01)	5.94 (0.18)	7.27 (0.09)
No multiscale downsampling	0.57 (0.01)	0.86 (0.02)	6.95 (0.25)	8.03 (0.12)

Table 1: Prediction performance of model variants and ablations, computed over moving chunks only. For all metrics, the mean over 5 model training seeds is shown with standard deviation in parentheses. The base model is YCB-100-100. All models use a prediction horizon of 4 at 10 Hz. We observe small prediction performance drops for variations in number of augmented scenes in the training data and splatting-specific properties. Stronger performance degradations are observed for a training set with small object pool and when not doing multiscale downsampling.

the data we are dealing with: even when one object experiences an interaction, other objects might not be affected and do not move at all. Secondly, a small change in actor movement can have drastic effect on an object trajectory: if it narrowly passes an object, the changes are zero, but if it hits the object, it might fall over and experience a rotation change in the order of magnitude of  $90^\circ$  and several cm of position change in under a second. We compare several model variants trained at different timestep granularities (5 Hz, 10 Hz) and prediction horizons (4, 8 and 12 steps). We observe that the determining factor for median prediction error in both position and rotation is the prediction horizon in time, where for the same horizon all variants perform relatively similarly.

**Model variants and ablations** In Table 1, we compare our main model trained on YCB-100-100 with prediction horizon 4 at 10 Hz with several ablations. Regarding the number of used training scenes and augmented layouts, we observe that using 100 training scenes with 100 layouts achieves slightly better position and rotation prediction performance than the other two combinations. Regarding the number of observed objects, we see that YCBV-100-100, which only draws from a pool of 16 objects, experiences strongest performance degradation. Using double or half the anchor resolution both leads to small performance losses. This appears natural for the more coarse resolution, since geometry has to be compressed into the same number of features at a coarser scale. For the finer resolution, we suspect the performance drop might be due to the spatial aggregation and downsampling in the transformer which now aggregates many anchors together without paying respect to their spatial layout. Conversely, for the default anchor scale, the geometry is encoded in the anchor features. Operating the transformer directly on decoded Gaussians instead of anchors also leads to small performance drops. A similar argument as for the small voxels applies: For

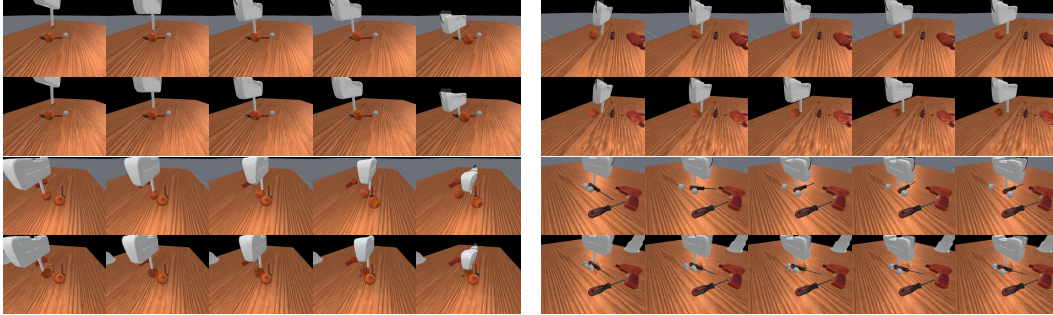


Figure 3: Predicted sequences over horizon 2.4 s (3 model invocations) and ground truth (atop predictions for each sequence) replayed in simulation. We select examples according to their combined prediction error rank from the top 10% quantile of pose changes (see text for details). Top row: Smallest and second smallest predicted error rank. Bottom left: Median error rank. Bottom right: Worst error rank. The object interactions are predicted closely to the ground truth for the two smallest error ranks. For the median and worst ranks, small deviations in the interactions between gripper and objects can cause large deviations in object motion and are harder to predict.

the small Gaussians, accurate geometry information would need to be extracted out of many small points, whereas they are available in compressed form in the anchors. Interestingly, the variant with limited camera views, i.e., only azimuths between 0 and 180°, performs almost as well as the normal model trained on a full 360° range of camera azimuths of the scene. We conclude that indeed the model learned to cope with missing or imprecise shape information. Regarding architectural ablations, removing the spatio-temporal attention layer leads to stronger performance drop, especially in position prediction. The biggest impact can be observed when using no incremental downsampling and aggregation of points, but directly aggregating all points per object. This is expected due to the complex geometry of objects in our datasets.

**Qualitative examples** In Figure 3, we show the rendered scene representations over time, both the ground truth trajectory replayed and the model predictions. For the latter, we show the splatted Gaussian representation with rigid transformations, similarly to how our model perceives the scene. To demonstrate examples from a range of performances, we firstly rank the accumulated position change (between each time step, summed over objects and time) inside of a ground truth chunk between 0 and 1 and proceed similarly for rotation change. We then only consider chunks within the top 10% of summed position and rotation change rank. Naturally speaking, this selects chunks with the highest amount of movement in position or rotation. We similarly rank the position and rotation prediction errors of our model over the chunks and show the (second) best, median and worst examples according to the summed error rank. In the examples, meaningful interactions can be observed, where for the ones with smallest rank the model predicts motion of a single round object which closely follows the ground truth. For the median example, the screwdriver rotation is underestimated. However, due to the contact near to the center of mass, this motion can be difficult to predict. The worst example shows a difficult multi-object interaction setting where a small change in end-effector position can result in a large change in object motion.

### 4.3 Planning Results

We evaluate the performance of our model (prediction horizon 8 at 5 Hz) in a model-predictive control setting on two tasks in Table 2. We observe that the goal is achieved in the majority of cases with higher success rates for the single-object tasks 1 (0.77 at success threshold distance 1 cm) than for task 2 (0.66 at success threshold distance 0 cm), where up to 5 objects have to be pushed outside of an area. Considering success per object individually in the latter task shows a higher success rate. Increasing the success threshold distances to 2 cm also increases success rates. Also, goal achievement metrics for both task are reduced compared to their values at the episode start. In Figure 4, we visualize successful episodes for both tasks on scenes of 5 objects with the largest initial objective value. In the task 1 example, the target screwdriver is successfully maneuvered to the goal. The task 2 example demonstrates how the robot pushes several objects together initially. We perform visual inspection of failed episodes for both tasks on scenes with five objects (for one model training seed) and identify

task	time to succ. in s	success rate (SR)	SR@2 cm	SR AUC	final goal dist. in cm	initial goal dist. in cm
1. push object to position	20.9 (0.6)	0.77 (0.02)	0.80 (0.03)	0.83 (0.03)	2.87 (0.38)	14.17
2. clear middle (all obj.)	26.7 (1.1)	0.66 (0.05)	0.72 (0.05)	0.68 (0.04)	3.12 (0.42)	30.4
clear middle (per obj.)		0.82 (0.03)	0.88 (0.02)	0.81 (0.02)		

Table 2: Planning performance on different tasks where our model is used in a MPC setting. All metrics are computed by taking the mean over all episodes for one training model seed. Final goal distance is measured at success or time out. Then, the mean over 5 model training seeds is computed and shown here, with standard deviation in parentheses. A majority of runs is successful and error metrics are reduced from their initial values. See appendix section B for details on used metrics.

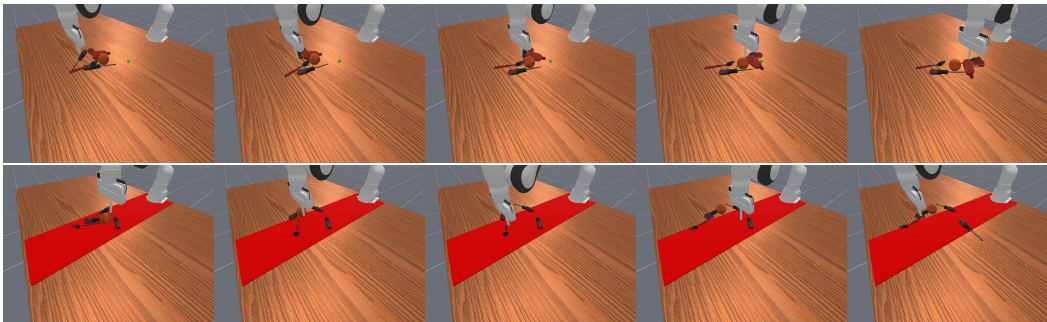


Figure 4: Examples for MPC performance with 5 objects and largest initial objective value. Top: push object to position (task 1). Bottom: clear middle (task 2). The tasks are successfully solved.

the following typical failure cases: In several cases the robot gets stuck when it reaches outside of the kinematic workspace of the robot arm. This failure is prone to happen if an object gets pushed close or beyond the kinematic workspace limits which is observed in multiple episodes of task 2. In some failed episodes of both tasks it is observed that the robot struggles to manipulate the screwdriver and the spoon, hinting on difficulty to accurately predict the movement of such elongated objects. In some cases of task 2, the robot switches several times between approaching different target objects, eventually running out of time. Such behavior could be alleviated by a more intricate design of the planning cost functions.

## 5 Conclusion and Limitations

We present MRO-GWM, a novel action-conditional world model that operates on an object-centric Gaussian splatting representation and predicts rigid body movement. The Gaussians are compressed in anchors which are represented in the object frames and are rigidly transformed to condition the model on a history of object poses. We further propose a spatio-temporal transformer architecture that operates on this representation and uses temporal and spatial attention blocks as well as a new spatio-temporal attention block. We evaluate our model on simulated tabletop scenes where up to five typical household objects are closely placed next to each other and interaction is caused by a robotic end effector. We compare prediction performance of several model variants and ablations of our architecture and find that a smaller view angle range of the scene only marginally decrease performance. Finally, we demonstrate that model-predictive control with our model can successfully tackle two non-prehensile manipulation tasks in simulation in several multi-object configurations. Limitations of the proposed approach are the assumption that object masks and pose estimates of the objects in the scene are known, which restricts the evaluation to synthetic datasets. This could be alleviated by integrating segmentation foundation models and pose trackers into the method in future work. We further only consider rigid-body dynamics which could be extended in future work by predicting object deformations, too. Improving the model or planning method for real-time control is also an avenue for future work.

## Acknowledgements

This work has been supported by Hightech Agenda Bayern and Deutsche Forschungsgemeinschaft (DFG) project no. 466606396 (STU 771/1-1). We gratefully acknowledge the HPC resources provided by the Erlangen National High Performance Computing Center (NHR@FAU) of the Friedrich-Alexander-Universität Erlangen-Nürnberg (FAU) under the BayernKI project v19ee. BayernKI funding is provided by Bavarian state authorities.

## References

- [1] Jad Abou-Chakra, Krishan Rana, Feras Dayoub, and Niko Suenderhauf. Physically embodied gaussian splatting: A visually learnt and physically grounded 3d representation for robotics. In *Proc. of the Conf. on Robot Learning (CoRL)*, 2025.
- [2] Takuya Akiba, Shotaro Sano, Toshihiko Yanase, Takeru Ohta, and Masanori Koyama. Optuna: A next-generation hyperparameter optimization framework. In *Proc. of the 25th ACM SIGKDD Int. Conf. on Knowledge Discovery and Data Mining*, 2019.
- [3] Jason Ansel, Edward Yang, Horace He, Natalia Gimelshein, Animesh Jain, Michael Voznesensky, Bin Bao, Peter Bell, David Berard, Evgeni Burovski, Geeta Chauhan, Anjali Chourdia, Will Constable, Alban Desmaison, Zachary DeVito, Elias Ellison, Will Feng, Jiong Gong, Michael Gschwind, Brian Hirsh, Sherlock Huang, Kshiteej Kalambarkar, Laurent Kirsch, Michael Lazos, Mario Lezcano, Yanbo Liang, Jason Liang, Yinghai Lu, CK Luk, Bert Maher, Yunjie Pan, Christian Puhersch, Matthias Reso, Mark Saroufim, Marcos Yukio Siraichi, Helen Suk, Michael Suo, Phil Tillet, Eikan Wang, Xiaodong Wang, William Wen, Shunting Zhang, Xu Zhao, Keren Zhou, Richard Zou, Ajit Mathews, Gregory Chanan, Peng Wu, and Soumith Chintala. PyTorch 2: Faster Machine Learning Through Dynamic Python Bytecode Transformation and Graph Compilation. In *29th ACM Int. Conf. on Architectural Support for Programming Languages and Operating Systems, Volume 2 (ASPLOS '24)*, 2024.
- [4] Jake Bruce, Michael D. Dennis, Ashley Edwards, Jack Parker-Holder, Yuge Shi, Edward Hughes, Matthew Lai, Aditi Mavalankar, Richie Steigerwald, Chris Apps, Yusuf Aytar, Sarah Bechtle, Feryal M. P. Behbahani, Stephanie C. Y. Chan, Nicolas Heess, Lucy Gonzalez, Simon Osindero, Sherjil Ozair, Scott E. Reed, Jingwei Zhang, Konrad Zolna, Jeff Clune, Nando de Freitas, Satinder Singh, and Tim Rocktäschel. Genie: Generative interactive environments. In *Proc. of the Int. Conf. on Machine Learning (ICML)*, 2024.
- [5] Berk Çalli, Aaron Walsman, Arjun Singh, Siddhartha S. Srinivasa, Pieter Abbeel, and Aaron M. Dollar. Benchmarking in manipulation research: Using the Yale-CMU-Berkeley object and model set. *IEEE Robotics Autom. Mag.*, 22(3), 2015.
- [6] Ying Chai, Litao Deng, Ruizhi Shao, Jiajun Zhang, Kangchen Lv, Liangjun Xing, Xiang Li, Hongwen Zhang, and Yebin Liu. GAF: Gaussian action field as a 4d representation for dynamic world modeling in robotic manipulation. In *IEEE Int. Conf. on Robotics and Automation (ICRA)*, 2026. To appear.
- [7] Filipe de Avila Belbute-Peres, Kevin A. Smith, Kelsey R. Allen, Josh Tenenbaum, and J. Zico Kolter. End-to-end differentiable physics for learning and control. In *Advances in Neural Information Processing Systems (NeurIPS)*, 2018.
- [8] Danny Driess, Zhiao Huang, Yunzhu Li, Russ Tedrake, and Marc Toussaint. Learning multi-object dynamics with compositional neural radiance fields. In *Proc. of the 6th Conference on Robot Learning (CoRL)*, 2023.
- [9] Andreas René Geist, Jonas Frey, Mikel Zbroto, Anna Levina, and Georg Martius. Learning with 3D rotations, a hitchhiker’s guide to SO(3). In *Proc. of the 41st Int. Conf. on Machine Learning (ICML)*, 2024.
- [10] Danijar Hafner, Timothy P. Lillicrap, Ian Fischer, Ruben Villegas, David Ha, Honglak Lee, and James Davidson. Learning latent dynamics for planning from pixels. In *Proc. of the Int. Conf. on Machine Learning (ICML)*, 2019.
- [11] Taylor Howell, Nimrod Gileadi, Saran Tunyasuvunakool, Kevin Zakka, Tom Erez, and Yuval Tassa. Predictive Sampling: Real-time Behaviour Synthesis with MuJoCo. *arXiv preprint arXiv:2212.00541*, 2022.
- [12] Yuanming Hu, Yu Fang, Ziheng Ge, Ziyin Qu, Yixin Zhu, Andre Pradhana, and Chenfanfu Jiang. A moving least squares material point method with displacement discontinuity and two-way rigid body coupling. *ACM Trans. Graph.*, 37(4), 2018.

- [13] Binbin Huang, Zehao Yu, Anpei Chen, Andreas Geiger, and Shenghua Gao. 2d gaussian splatting for geometrically accurate radiance fields. In *SIGGRAPH 2024 Conference Papers*, 2024.
- [14] Bernhard Kerbl, Georgios Kopanas, Thomas Leimkühler, and George Drettakis. 3d gaussian splatting for real-time radiance field rendering. *ACM Transactions on Graphics*, 42(4), 2023.
- [15] Albert H. Li, Brandon Hung, Aaron D. Ames, Jiuguang Wang, Simon Le Cleac’h, and Preston Culbertson. Judo: A user-friendly open-source package for sampling-based model predictive control. In *Proc. of the Workshop on Fast Motion Planning and Control in the Era of Parallelism at Robotics: Science and Systems (RSS)*, 2025.
- [16] Shiqian Li, Ruihong Shen, Junfeng Ni, Chang Pan, Chi Zhang, and Yixin Zhu. Learning physics-grounded 4d dynamics with neural gaussian force fields. In *Proc. of the Int. Conf. on Learning Representations (ICLR)*, 2026.
- [17] Wenxuan Li, Hang Zhao, Zhiyuan Yu, Yu Du, Qin Zou, Ruizhen Hu, and Kai Xu. PIN-WM: Learning physics-informed world models for non-prehensile manipulation. *arXiv preprint arXiv:2504.16693*, 2025.
- [18] Ilya Loshchilov and Frank Hutter. Decoupled weight decay regularization. In *Proc. of the Int. Conf. on Learning Representations (ICLR)*, 2019.
- [19] Guanxing Lu, Shiyi Zhang, Ziwei Wang, Changliu Liu, Jiwen Lu, and Yansong Tang. ManiGaussian: Dynamic gaussian splatting for multi-task robotic manipulation. In *Proc. of the European Conf. on Computer Vision (ECCV)*, 2024.
- [20] Guanxing Lu, Baoxiong Jia, Puhao Li, Yixin Chen, Ziwei Wang, Yansong Tang, and Siyuan Huang. GWM: Towards scalable gaussian world models for robotic manipulation. *Proc. of Int. Conf. on Computer Vision (ICCV)*, 2025.
- [21] Tao Lu, Mulin Yu, Linning Xu, Yuanbo Xiangli, Limin Wang, Dahua Lin, and Bo Dai. Scaffold-GS: Structured 3d gaussians for view-adaptive rendering. In *Proc. of the IEEE/CVF Conf. on Computer Vision and Pattern Recognition (CVPR)*, 2024.
- [22] Shaohui Pan, Yong Xu, Ruotao Xu, Zihan Zhou, Si Wu, and Zhuliang Yu. Self-correcting robot manipulation via gaussian-splatted foresight. In *Proc. of the Thirty-Ninth AAAI Conf. on Artificial Intelligence and Thirty-Seventh Conf. on Innovative Applications of Artificial Intelligence and Fifteenth Symposium on Educational Advances in Artificial Intelligence*, 2025.
- [23] William Peebles and Saining Xie. Scalable diffusion models with transformers. *arXiv preprint arXiv:2212.09748*, 2022.
- [24] Corrado Pezzato, Chadi Salmi, Elia Trevisan, Max Spahn, Javier Alonso-Mora, and Carlos Hernández Corbato. Sampling-based model predictive control leveraging parallelizable physics simulations. *IEEE Robotics and Automation Letters*, 10(3), 2025.
- [25] Cristina Pinneri, Shambhuraj Sawant, Sebastian Blaes, Jan Achterhold, Joerg Stueckler, Michal Rolinek, and Georg Martius. Sample-efficient cross-entropy method for real-time planning. In *Proc. of the 2020 Conference on Robot Learning (CoRL)*, 2021.
- [26] Stone Tao, Fanbo Xiang, Arth Shukla, Yuzhe Qin, Xander Hinrichsen, Xiaodi Yuan, Chen Bao, Xinsong Lin, Yulin Liu, Tse kai Chan, Yuan Gao, Xuanlin Li, Tongzhou Mu, Nan Xiao, Arnav Gurha, Viswesh Nagaswamy Rajesh, Yong Woo Choi, Yen-Ru Chen, Zhiao Huang, Roberto Calandra, Rui Chen, Shan Luo, and Hao Su. Maniskill3: GPU parallelized robotics simulation and rendering for generalizable embodied ai. *Robotics: Science and Systems*, 2025.
- [27] Wei-Cheng Tseng, Ellina Zhang, Krishna Murthy Jatavallabhula, and Florian Shkurti. Gaussian splatting visual MPC for granular media manipulation. In *Proc. of the IEEE Int. Conf. on Robotics and Automation (ICRA)*, 2025.
- [28] Ashish Vaswani, Noam Shazeer, Niki Parmar, Jakob Uszkoreit, Llion Jones, Aidan N Gomez, Łukasz Kaiser, and Illia Polosukhin. Attention is all you need. In *Advances in Neural Information Processing Systems (NeurIPS)*, 2017.
- [29] Meizhong Wang, Wanxin Jin, Kun Cao, Lihua Xie, and Yiguang Hong. ContactGaussian-WM: Learning physics-grounded world model from videos. *arXiv preprint arXiv:2602.11021*, 2026.
- [30] Xiaoyang Wu, Yixing Lao, Li Jiang, Xihui Liu, and Hengshuang Zhao. Point transformer v2: Grouped vector attention and partition-based pooling. In *Advances in Neural Information Processing Systems (NeurIPS)*, 2022.

- [31] Yu Xiang, Tanner Schmidt, Venkatraman Narayanan, and Dieter Fox. PoseCNN: A convolutional neural network for 6d object pose estimation in cluttered scenes. In *Proc. of Robotics: Science and Systems (RSS)*, 2018.
- [32] Tianyi Xie, Zeshun Zong, Yuxing Qiu, Xuan Li, Yutao Feng, Yin Yang, and Chenfanfu Jiang. PhysGaussian: Physics-integrated 3d gaussians for generative dynamics. In *Proc. of the IEEE/CVF Conf. on Computer Vision and Pattern Recognition (CVPR)*, 2024.
- [33] Tengbo Yu, Guanxing Lu, Zaijia Yang, Haoyuan Deng, Season Si Chen, Jiwen Lu, Wenbo Ding, Guoqiang Hu, Yansong Tang, and Ziwei Wang. Manigaussian++: General robotic bimanual manipulation with hierarchical gaussian world model. In *Proc. of the IEEE/RSJ Int. Conf. on Intelligent Robots and Systems (IROS)*, 2025.
- [34] Mingtong Zhang, Kaifeng Zhang, and Yunzhu Li. Dynamic 3d gaussian tracking for graph-based neural dynamics modeling. In *Proc. of the Conf. on Robot Learning (CoRL)*, 2024.
- [35] Tianyuan Zhang, Hong-Xing Yu, Rundi Wu, Brandon Y. Feng, Changxi Zheng, Noah Snavely, Jiajun Wu, and William T. Freeman. PhysDreamer: Physics-based interaction with 3d objects via video generation. In *Proc. of the European Conf. on Computer Vision (ECCV)*, 2024.
- [36] Haoyu Zhao, Hao Wang, Xingyue Zhao, Hao Fei, Hongqiu Wang, Chengjiang Long, and Hua Zou. Efficient physics simulation for 3D scenes via mllm-guided gaussian splatting. *arXiv preprint arXiv:2411.12789*, 2025.
- [37] Mikel Zbrobo, Andreas René Geist, and Georg Martius. Learning 3D-Gaussian simulators from RGB videos. *arXiv preprint arXiv:2503.24009*, 2025.
- [38] Ruijie Zhu, Mulin Yu, Linning Xu, Lihan Jiang, Yixuan Li, Tianzhu Zhang, Jiangmiao Pang, and Bo Dai. ObjectGS: Object-aware scene reconstruction and scene understanding via gaussian splatting. In *Proc. of the Int. Conf. on Computer Vision (ICCV)*, 2025.

## A Dataset Details

**Scene generation** For our train and val datasets, we sample the object count uniformly between 1 and 5. For our test datasets, we create equal parts of scenes with object counts from 1 to 5. We then sample the object models according to the corresponding split as detailed in Section 4.1. We sample position and rotation for objects one after the other. For all considered objects, we define meaningful ways how they can be rotated to approximate typical orientations in household environments. For example, a box-like object can lie on any of its 6 faces and then be rotated arbitrarily along the world z axis. A round object like a golf ball can have arbitrary rotation. To this end, we determine an orientation category for each and sample the orientations accordingly. The following categories exist:

- "standing", e.g. cans. always point up, no orientation sampling (except for a random yaw later).
- "box-like", e.g. cracker box. can stand on any of its 6 faces
- "cylindrical", e.g. screwdriver. Has an arbitrary rotation axis that does not coincide with yaw after positioning.
- "any", e.g. balls. fully arbitrary orientation.
- "power drill". For this particular object, we sample whether it should stand up or lay on one side by a fair coin toss.

Note that due to interaction with the robot, standing objects can be toppled over. After potentially sampling a possible orientation, we apply a random yaw rotation before placing the object on the table. We then sample a position in an area of  $40 \times 40$  cm and check for collisions, potentially rejecting the placement. We let the scene settle by simulating several steps and then try to bring the objects closely together. To this end, we lift all objects in the air, lock all by the x and y motion axes, apply a force towards the origin to each object and simulate several steps while increasing the linear damping. This pushes the object closely together. We then lower the damping again and let the scene settle. We choose the described sampling scheme to produce typical and interesting orientations, which would be unlikely by fully random 3D orientation sampling (e.g., standing up).

**Occlusion filtering** Naively, our sampling process might produce scenes where some objects are heavily occluded. We therefore perform the following check to ensure each object is to some degree visible from multiple views: For each camera view and object, we render it together with all other objects and once with other objects made invisible. We count how many pixels can be observed in the first case as  $n_o$  ("potentially occluded") and with all other objects invisible as  $n_u$  ("unoccluded"). Their fraction is the occlusion fraction  $f = n_o/n_u$ . We check whether  $f \geq 0.5$  and if  $n_u \geq 1024$ . The second requirement ensures that the object covers a significant portion of the image ( $1024 = 32 \cdot 32$ ), where our images are  $1280 \times 720$ . We require that this constraint holds in at least 25% of views for each object. Otherwise, the scene is discarded.

**Interaction data generation** To collect interaction data, we select one target object randomly. For this target object, we select a target point between its bounding box and its bounding box enlarged by a factor of 1.2. This point is subsequently targeted by the robot end-effector from its current position. This scheme leads to trajectories where the robot is always in the vicinity of objects, sometimes going around them and sometimes interacting with them (for example by sampling a point on the opposite side of the object). Using the distance between the current position and the target point and a target end-effector speed of 5 cm/s, a number of linear interpolation points matching the control frequency is determined and subsequently sent as actions to a low-level PD controller. These actions (interpolated target end-effector positions) are recorded and serve as input to our dynamics model. The resulting poses of the objects are also recorded and serve as ground-truth training data. The control frequency with the simulation is 20 Hz, but our models operate on a coarser timescale of 10 Hz or 5 Hz, for which the recorded data points are sliced. We filter out extreme behavior where object speeds exceed 0.8 m/s and rotational velocities  $6\pi$  rad/s and re-sample the layout in this case.

## B Details on Sampling-Based Planning Evaluation

**Task specification** In task 1 "push object to position", a random object is selected and a 2D goal position is sampled randomly in the interval  $[-15 \text{ cm}, 15 \text{ cm}]$  for both axes. There are no constraints

on the movement of other objects. We evaluate the Euclidean distance of object center to goal position and denote an episode as successful if this falls below 1 cm. In Table 2, we additionally evaluate the success rate if the distance threshold is increased to 2 cm. We also provide an area-under-curve (AUC) metric, where success is determined with multiple thresholds ranging from 1 cm to 5 cm in 5 mm steps and the average is taken over those. The cost terms evaluated at each planning iteration are as follows: The main cost is the Euclidean distance between the selected object and its goal position averaged over the number of rollout steps. A secondary cost is the Euclidean distance between the end effector and the selected object, averaged over the number of rollout steps and weighted by 0.05. A quadratic loss is applied to the end-effector-object distance once it falls below the threshold of 10 cm. This low-weighted cost is used to shape the exploration to attract the end-effector to the selected object to increase the ratio of meaningful interaction within the limited planning horizon.

In task 2 "clear middle", all objects shall be moved outside the interval  $[-15 \text{ cm}, 15 \text{ cm}]$  on the y-axis, which spans the central part of the table. We evaluate the smaller distance from object center to either bound and sum these up for all objects as goal distance. Success is determined on zero distance to bounds for all objects. In Table 2, we additionally analyze success per object individually (zero distance to bounds) and success if a larger than zero distance to bounds is allowed. For the latter, we provide success rates at 2 cm threshold and also an AUC metric, where the mean over thresholds from 0 cm to 5 cm in 5 mm steps is taken.

The cost terms evaluated at each planning iteration are as follows: The main cost is the sum of distances between each object and the closest interval bound for all objects inside the interval averaged over the number of rollout steps. A secondary cost is the sum of Euclidean distances between the end effector and each object inside the interval, averaged over the number of rollout steps and weighted by 0.05. A quadratic loss is applied to end-effector-object distances that fall below the threshold of 10 cm. This guides the exploration towards remaining objects in the interval until it is cleared. We also include a cost term to penalize pushing objects too far off the table center without improving on the clearance objective. The corresponding cost is the sum of distances of objects from the closest bound of the workspace interval  $[-15 \text{ cm}, 15 \text{ cm}]$  along the x-axis, averaged over the number of rollout steps and weighted by 0.1.

As detailed in the next section, the planned actions are represented as keypoints which are interpolated to execute the motion. Additionally both tasks share the same two keypoint-based objectives that incentivize the keypoint-distribution to stay within the reachable horizon of the interpolated trajectory and prohibit it to drift below the surface of the table. We run episodes for both tasks for 1200 environment steps, which corresponds to 1 min.

**Planning method** Our planning framework is similar to other sampling-based MPC frameworks that optimize keypoint-parametrized trajectories for robot control [24, 11, 15]. The single set of parameters reported in Sec. C is used in all experiments.

At each planning iteration a set of keypoint sequences is sampled from the CEM distribution parametrized by the keypoint mean and the isotropic keypoint covariance. The current position of the end effector is used to initialize the keypoint mean in the first planning iteration and is prepended as a starting keypoint to each sampled keypoint sequence subsequently. Each keypoint sequence is linearly interpolated and evaluated at a fixed number of 20 steps to obtain a trajectory of dense end-effector positions. The distance between consecutive positions on the trajectory is determined by the time difference required to match the step frequency of the model (5 Hz) and the constant end-effector velocity of 5 cm/s that is the same as in the training data. Note that a fixed number of consecutive positions spaced with a constant velocity might exceed or not cover the full linearly interpolated keypoint path. All positions beyond the last keypoint are kept at the last keypoint. A scalar cost is computed for each sampled keypoint sequence by evaluating the associated model rollout with a set of task-specific cost functions. An elite set of keypoint sequence samples is selected as the subset associated with the lowest cost. The keypoint mean of the normal distribution is updated with the mean of the keypoint sequences in the elite set and the keypoint sequence with the overall smallest cost is returned as the planning result as proposed in iCEM [25]. If after the update the mean associated with the first keypoint in a sequence is within execution range of the robot from the current position the keypoint mean is shifted by one sequence index to prevent sampling the first keypoint from a distribution centered around the starting keypoint at the next planning iteration. This shift is inspired by the shift of the action sequence distribution described in iCEM [25] but is adapted to happen on the coarser scale of trajectory keypoints instead of the dense scale of trajectory steps. Since

model rollouts are compute intensive and the cost landscape changes between each planning iteration, only a single optimization iteration is performed that updates the mean but not the covariance. In the case of a single optimization iteration that never resets the covariance, it is beneficial to not update the covariance to maintain a constant exploration and prevent the collapse of the CEM distribution.

## C Hyperparameters

**Model architecture details** For the residual blocks in our transformer, we also follow the architecture of DiT in applying a layer norm before each layer and AdaLN-like [23] modulation, albeit with constant conditioning. We also apply the a DiT style final layer and use their initialization scheme.

**Splatting details and parameters** For our object-aware Gaussian splatting, we use the same hyperparameters as the "3dovs" configuration of ObjectGS with the following modifications: We use the 2D Gaussian splatting mode and train for only 5000 steps. Our default voxel size is 0.01, i.e., 1 cm, and we use 5 Gaussians per anchor. To splat the scenes, we use `lambda_dreg=100` while to splat the end effector we use `lambda_sky_opa=1`. These parameters were selected in preliminary experiments. E.g `lambda_dreg=100` ensures that Gaussians are unlikely to be placed in unobserved areas, which would introduce strong visual artifacts when transformed as in our method. As mask for the optimization, we use the segmentation information from the simulator. If the ground or sky is hit, that part of the image is not used for optimization. For our splatting with shared MLPs, we accumulated gradients and update the MLP every 50 steps. We step through all scenes in order and select one random view for each, without replacement. After several passes, all cameras have been selected and we make all cameras available for sampling again.

**Model hyperparameters** We embed the object index with dimension 8 and whether the timestep is in history or prediction with dimension 4 into each point. We clip gradients at 1. We tried out a constant learning rate but found the cosine schedule to perform better. For the rotation representation, we additionally compared an axis-angle representation (rotation axis unit vector scaled by rotation amount around the axis). For rotation loss, we compared the l2-norm on the vectors and a geodesic angle error. The variant described in the paper produced best results. To combine position and rotation loss terms, we use a factor of 1 for position and a factor of 0.5 for rotation. For the spatial attention from PTv2, we use the spatial attention bias but not the attention multiplier. We found this combination to perform best and use the same for spatio-temporal attention. We use 16 neighbors for spatial attention. The parameters described so far were found in preliminary experiments with small model sizes and short runtimes (15k steps). Starting with an initial combination obtained mostly from defaults from work we build on, we ran experiments with independently changed parameters. If a parameter change indicated a clear improvement, we selected that value in a greedy fashion.

In a second stage, we optimized the structural parameters of the model, that means the number of stages, initial pool grid size and reduction factor per stage as well as initial feature size and increase factor per stage. The depth (number of blocks per stage) was set to one. To this end, we ran a parameter optimization with Optuna [2] with 107 random runs and 50 runs sampled with TPESampler (`multivariate=True, group=True`). We used a multi-objective with position and rotation loss and ran the training for 20k steps. Trials were pruned after a timeout of 6 hours or going out of memory on an Nvidia A40. We selected all parameters on the pareto front and conducted training for 60k steps and depths of 1 and 2. We selected the best performing combination of this with the following parameters:

- Grid sizes (computed from initial value and decrease factor): 0.019,0.031,0.049,10 where the last stage aggregates all points per object
- Feature sizes (computed from initial value and increase factor): 48,88,160,296
- Depth 2

Regarding number of training steps and batch size, we did not observe a significant performance increase when increasing training to 100k steps and batch size to 40.

**Planning hyperparameters** For the planning experiments, we optimized planning parameters by hand on the clear middle task and used the fraction of objects that were successfully pushed

beyond the bounds as objective metric. We ran planning on the validation set scenes (20) with 10 episodes each. Starting from a parameter set from preliminary experiments, we assumed parameters as independent and tried out several different settings from the current values. If we observed a clear best setting for a value with satisfactory resolution, we adopted this value as new default. Otherwise, the previous value was kept and potentially other values tested for the next iteration. After 3 iterations, we determined the following values:

- Model variant (out of prediction horizon 4, 8, 12, all operating at 5 Hz): prediction horizon 8
- CEM  $\sigma = 0.02$
- CEM number of elites: 4
- Number of parallel rollouts: 96
- Planning horizon (in model steps): 20
- Replanning frequency (in environment steps): 10

## **D Details of Used GPU Hardware**

As stated in the main paper, our main model takes approximately 22 h as a job on a cluster node with one Nvidia A40 GPU to train. The cluster nodes feature the following hardware: 2 x AMD EPYC 7713 ("Milan", "Zen3"), 2 x 64 cores @2.0 GHz, 512 GB main memory, of which a single job may use 16 cores and 60 GB memory. The prediction experiments take approximately 15 min on such a node for the base model. Training models with longer prediction horizon requires more GPU memory. We trained those variants on a cluster node with one Nvidia H100 GPU. Those nodes feature the following hardware: 2 x AMD EPYC 9554 ("Genoa", "Zen4"), 2 x 64 cores @3.1 GHz, 768 GB main memory, of which a single job may use 32 cores and 192 GB memory. The model with prediction horizon 12 trained for approximately 22 hours on such a node. We conduct the planning experiments all on nodes with A40, where planning for one scene takes between 45 min and 90 min for most runs.